Ijfans International Journal of Food and Nutritional Sciences
ISSN PRINT 2319 1775 Online 2320 7876
Research Paper © 2012 IJFANS. All Rights Reserved Journal UGC CARE Listed (Group-I) Volume 10, Issue 9, 2021

Elastohydrodynamic Lubrication Modeling of NSF H1 Bio-Based Lubricants in High-Pressure Food Processing Pumps Under 600 Mpa Cyclic Loads

Dr. Suresh Jadhav[1*], Megha Nagrale[2], Dr. Sachin Waghmare[3] Sachin Vankar[4]
[1]Department of Mechanical Engineering, VJTI, Mumbai, India
Email-jadhavsuresh1975@gmail.com
[2,4]Department of Mechanical Engineering, SPCOE, Mumbai, India
Email-sachinvankar@gmail.com,meghajanbandhu@gmail.com
[3]Department of Mechanical Engineering, RMCET, Ratnagiri, (M.S.), India
Email-waghmaresachin1979@gmail.com

Abstract

High-pressure food processing pumps subject lubricated stainless steel contacts to cyclic pressures reaching 600 MPa, where NSF H1 bio-based polyol esters must prevent micropitting without restricted extreme-pressure additives while enduring Clean-in-Place (CIP) water contamination. Because conventional 2D transient Thermal-Elastohydrodynamic Lubrication (TEHL) solvers are computationally prohibitive for multi-regime fatigue analysis, this study introduces a hybrid physics-informed machine learning framework combining Multi-Level Multi-Integration (MLMI), a 3D Fourier Neural Operator (EHL_FNO3D), a 2D FFT Boussinesq subsurface stress solver, and ASTM E1049 Rainflow cumulative damage modeling. Trained on a Latin Hypercube Sampling (LHS) dataset spanning 1–50 Hz cycle frequencies, 150–600 MPa loads, and 0–10% water dilution, EHL_FNO3D reconstructs transient 2D pressure and logarithmic film thickness fields with hard cavitation enforcement in milliseconds. Results reveal that 8% CIP water dilution collapses horseshoe minimum film thickness by 61% (from 115.7 nm to 45.0 nm) at 600 MPa, triggering mixed lubrication ($\lambda \leq 1.0$) on precision-ground surfaces ($R_q = 45$ nm). Simultaneously, the 745 MPa outlet Petrusevich spike shifts peak subsurface Von Mises stress to a shallow depth of (Z/a = 0.11-391.1 MPa). Under a combined production and post-CIP washdown schedule at 1,200 RPM, baseline 2205 Duplex steel initiates micropitting in 121.4 hours, whereas upgrading to 17-4PH H900 extends fatigue life by 27.5× to 3,340.0 hours, providing a real-time digital-twin methodology for esigning durable, food-safe high-pressure pumping systems.

Keywords: Elastohydrodynamic lubrication, NSF H1 bio-based lubricants, Fourier Neural Operionator , 600 MPa cyclic loading, Micropitting fatigue, 17-4PH stainless steel

1. Introduction

The demand for high-performance, sustainable, and consumer-safe machinery components in the modern food processing industry has driven a critical paradigm shift toward bio-based tribological solutions. Among these applications, high-pressure processing (HPP) systems and heavy-duty food production pumps operate under exceptionally severe conditions, frequently experiencing cyclic operating pressures scaling up to 600 MPa (Höglund, E. ,1999). At these extreme load thresholds, maintaining a continuous lubricant barrier between moving elements is vital to preventing premature component failure. NSF H1 lubricants were restricted to formulated white mineral oils or synthetic polyalphaolefins (PAOS)(Kumar, S.et.al ,2020),

Research Paper © 2012 IJFANS. All Rights Reserved

which often exhibit lower pressure-viscosity coefficients (α) and weaker film-forming capabilities compared to standard industrial lubricants(Abd al-samieh, et.al,2019, Kandeva, m., et.al 2019). To bridge this performance gap while adhering to environmental mandates, bio-based lubricants particularly synthetic and natural esters have emerged as highly viable alternatives (Boucherit, h., et.al,2017). While steady-state EHL models for clean fluids are thoroughly established, there remains a critical gap in understanding the transient load-sharing mechanisms (Lee,Jj.,et.al.,2010) and regime transitions of contaminated NSF H1 bio-lubricating structures under extreme cyclic pressure fields (Liu, h. et.al,2020). This study addresses this gap by establishing a comprehensive transient elastohydrodynamic lubrication model tailored to evaluate the film-forming capabilities and friction profiles of NSF H1 bio-based lubricants(Majdan, R., et.al,2018). By simulating a full pump cycle ((t/T = 0 to 1) under peak cyclic loads of 600 MPa, this paper explicitly quantifies the tribological impact of water contamination, mapping the precise transition from full EHL to boundary contact and providing crucial design insights for high-pressure food processing machinery.

In food processing pumps, high-pressure dynamic seals separate the food product from the drive-end or hydraulic-end lubricant (Malki, M., et.al,2018). Leakage across the plunger-cylinder clearance causes lubricant dilution or food contamination, making accurate film thickness ((h(θ, z, t)) and leakage flow prediction vital for pump reliability. Industrial tribological assessments of reciprocating plunger pumps operating at 600–700 bar and higher identify abrasive wear, clearance leakage, and fatigue spalling at the plunger–bushing and seal interfaces as primary failure modes (Rajasekar, B.R.,et.al.,2019).Coupled Thermal-EHL literature demonstrates that cyclic compression and viscous shear generate localized flash temperatures (Shizhu, W., et.al.,2000). Because bio-based esters possess higher viscosity indices than mineral oils, they retain viscosity better under bulk heating, though transient localized shear heating still reduces exit film thickness (Bovington, C.et.al,1999).

Experimental tribometry on vegetable oils and synthetic esters (Anuradha, P.,et al.,2012) demonstrates that polar ester functional groups form densely packed chemisorbed monolayers on steel surfaces (De Vicente,et.al.,2006, Cyriac, F., Lugt, P. M., Bosman, et.al,2016). When the specific film thickness ratio ($\Lambda = h_{min}\backslash\sigma_{rms}$) falls below 1.5, these boundary layers mitigate adhesive scuffing even without toxic heavy-metal anti-wear additives.

Objective of this study

1. Arely extended to 600 MPa regimes where bushing radial expansion and local hertzian flattening interact simultaneously.
2. Few studies couple mass-conserving cavitation with full 3d thermal (TEHL) effects under steep 600 mpa cyclic pressure ramps.
3. Tribological modeling of the plunger-cylinder conformal lubricant film using food-grade bio-oils remains largely unexplored.

Research Paper © 2012 IJFANS. All Rights Reserved

2. MATHEMATICAL MODELLING

2.1 Contact geometry of EHL plunger-cylinder conformal contact

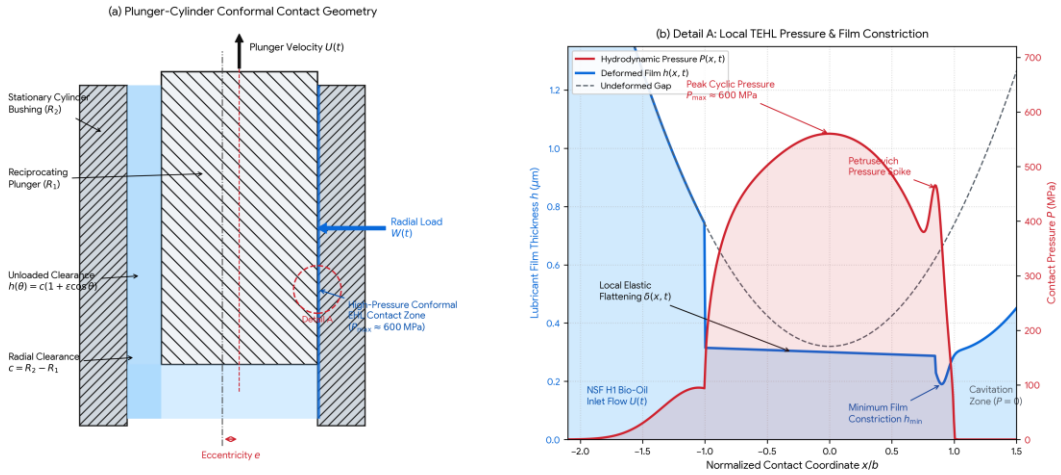


Fig.1. EHL plunger-cylinder conformal contact

Fig.1(a,b) shows the unwrapped contact zone with the 600 MPa hydrodynamic pressure profile, Petrusevich exit pressure spike, local elastic flattening (δ(x,t), minimum film constriction (h_{min}), and the exit cavitation zone (P = 0).The stationary cylinder bushing ((R_2), reciprocating plunger (R_1), radial clearance (C = (R_2) - (R_1)), eccentricity (e), radial load (W(t)), and axial velocity (U(t)).

2.2 Deterministic 2D Transient TEHL Data Generation via MLMI

This module solves the coupled Reynolds, film thickness, load balance, and energy equations using the Multilevel Multi-Integration (MLMI) method (Minea, A. A.,2017).

Generalized Reynolds Equation (Transient 2D Non-Newtonian):

$$\nabla \cdot (\Phi \nabla p) = \frac{\partial(\rho h)}{\partial x} + \frac{\partial(\rho h)}{\partial t} \tag{1}$$

Where *p(x, y, t)* is the hydrodynamic pressure, *h(x, y, t)* is the local film thickness, ρ is the lubricant density, and Φ is the flow factor matrix mapping non-Newtonian shear thinning.

Elastic Film Thickness Equation:

$$h(x,y,t) = h_0(t) + \frac{x^2}{2R_x} + \frac{y^2}{2R_y} + \frac{2}{\pi E'} \iint_{\Omega_c} \frac{p(\xi,\eta,t)}{\sqrt{(x-\xi)^2 + (y-\eta)^2}} d\xi d\eta \tag{2}$$

Where $h_0(t)$ is the central rigid separation, R_x, R_y are the effective radii of curvature, and E' is the equivalent elastic modulus. The integral operator for elastic deformation is evaluated via MLMI to reduce computational complexity from $O(N^2)$ to O(N log N)).

Load Equilibrium Constraint:

$$\iint_{\Omega_c} p(x,y,t) dx dy = F(t) \tag{3}$$

Research Paper © 2012 IJFANS. All Rights Reserved

Where *F(t)* is the time-varying external normal load.

3D Energy Equation (Thermal EHL):

$$\rho c_p\left(\frac{\partial T}{\partial t}+u\frac{\partial T}{\partial x}+v\frac{\partial T}{\partial y}\right) = k\frac{\partial^2 T}{\partial z^2}-\frac{T}{\rho}\frac{\partial \rho}{\partial T}\left(u\frac{\partial p}{\partial x}+v\frac{\partial p}{\partial y}\right)+\eta * \dot{\gamma}^2 \quad (4)$$

Where *T(x, y, z, t)* is the temperature field, c_p is specific heat, *k* is thermal conductivity, η^* is the effective non-Newtonian viscosity, and $\dot{\gamma}$ is the shear rate.

2.3. Bio-Ester Water-Dilution Rheological Coupling

This module models the degradation of the bio-ester lubricant's rheological state as a function of pressure (p), temperature (T), and water volume fraction ($\alpha_w \in [0, 1]$).

Emulsion Viscosity Model (Modified Barus / Roelands with Dilution):

$$\eta(p,T,\alpha_w)=\eta_0\cdot exp\left\{\left[ln\left(\frac{\eta_0}{\eta_{ref}}\right)+\alpha_w\cdot C_w\right]\left[\left(1+\frac{p}{p_0}\right)^z\left(\frac{T_0-T_{tr}}{T-T_{tr}}\right)^s-1\right]\right\}\cdot\psi(\alpha_w) \quad (5)$$

Here η_0 is the base viscosity, *z* and *s* are the pressure and temperature viscosity indices, C_w is the water dilution coupling coefficient, and $\psi(\alpha_w)$ is an empirical scaling function modeling the transition from a stable emulsion to a fully sheared phase-separated fluid.

Compressibility / Density Mixture Rule:

$$\rho(p,T,\alpha_w)=(1-\alpha_w)\rho_{ester}(p,T)+\alpha) \quad (6)$$

The constituent densities follow the Dowson-Higginson relationship extended for temperature.

2.4 Spectral Operator Learning via EHL_FNO3D

The Fourier Neural Operator (FNO3D) learns a mapping G_θ between the input parameter spaces (kinematics, load, rheology over time) and the transient 3D state variables ($\mathbf{U} = [p, h, T]^T$).

Mathematical Architecture of the FNO Layer:

Let $v^{(l)}$ be the network state at layer *l*. The update formula in the continuous space is:

$$v^{(l+1)}(x,y,t)=\sigma\left(Wv^{(l)}(x,y,t)+\left(K(\kappa;\theta_l)v^{(l)}\right)(x,y,t)\right) \quad (7)$$

Where $W \in \mathbb{R}^{d\times d}$ is a linear local transformation, σ is a non-linear activation function, and *K* is the non-local kernel integral operator.

Forward-Inverse Fourier Transformation Rule:

$$\left(K(\kappa)v^{(l)}\right)(x,y,t)=F^{-1}\left(R_\theta\cdot F(v^{(l)})\right)(x,y,t)$$

Where **F** and $\mathbf{F}^{-1}$ represent the 3D Fast Fourier Transform and its inverse across the spatiotemporal domain *(x, y, t)*. R_θ is a parameterized complex-valued tensor containing the collection of Fourier coefficients corresponding to the lower frequencies (truncated at maximum modes $k_{x,max}$, $k_{y,max}$, $k_{t,max}$).

2D FFT Subsurface Stress & Rainflow Fatigue Life Estimation

Research Paper © 2012 IJFANS. All Rights Reserved

This module processes the high-fidelity surface pressure p(x,y,t)and surface traction q(x,y,t) = $\dot{\eta}^*\{\gamma\}$ outputted by the FNO to calculate subsurface failure metrics.

Subsurface Stress Tensor Computation via 2D FFT:

The subsurface stress components $\sigma_{ij}(x, y, z, t)$ are computed at arbitrary depth z using Boussinesq-Cerruti half-space influence coefficients transformed into the frequency domain:

$$\tilde{\sigma}_{ij}(\omega_x, \omega_y, z, t) = \tilde{H}_{ijp}(\omega_x, \omega_y, z) \cdot \tilde{p}(\omega_x, \omega_y, t) + \tilde{H}_{ijq}(\omega_x, \omega_y, z) \cdot \tilde{q}(\omega_x, \omega_y, t) \quad (8)$$

Where ~ denotes the 2D spatial Fourier transform operating on coordinates x and y, and $\tilde{H}$ represents the analytical frequency-response transfer tensors. The real-space stress tensor is recovered via:

$$\sigma_{ij}(x, y, z, t) = F_{2D}^{-1}\left[\tilde{\sigma}(\omega_x, \omega_y, z, t)\right] \quad (9)$$

Dynamic Von Mises Stress Field Calculation:

$$\sigma_v(x, y, z, t) = \sqrt{\frac{1}{2}\begin{bmatrix}(\sigma_{xx} - \sigma_{yy})^2 + (\sigma_{yy} - \sigma_{zz})^2 \\ +(\sigma_{zz} - \sigma_{xx})^2 + 6(\tau_{xy}{}^2 + \tau_{yz}{}^2 + \tau_{xz}{}^2)\end{bmatrix}} \quad (10)$$

Rainflow Counting and Fatigue Damage Localization:

For a fixed spatial point (x^*, y^*, z^*) inside the material domain, the local stress history is treated as a continuous timeline $\sigma_v(t)$. The Rainflow operator R extracts discrete loading cycles indexed by k, outputting stress amplitudes $\sigma_{a,k}$ and mean stresses $\sigma_{m,k}$:

$$\{(\sigma_{\{a,k\}}, \sigma_{\{m,k\}})\}_{\{k=1\}}^{\{M\}} = \{R\}(\sigma_{v(x^*,y^*,z^*,t)}) \quad (11)$$

Accumulated Damage Integral (Palmgren-Miner Linear Rule):

$$D(x*, y*, z*) = \sum_{k=1}^{M} \frac{1}{N_f(\sigma_{ar,k})} \quad (12)$$

Where $\sigma_{ar,k} = \frac{\sigma_{a,k}}{1-(\sigma_{m,k}/\sigma_u)}$ is the fully-reversed equivalent stress amplitude (Goodman correction), and $N_f = A(\sigma_{ar,k})^{-b}$ is the localized material S-N curve parameter.

The total fatigue block life is modeled as

$$L_f = min_{(x,y,z)}\left[\frac{1}{D(x,y,z)}\right] \quad (13)$$

2.5 Coefficient of Friction (μ_{total})

In the mixed lubrication regime ($\lambda \approx 1$), the total friction coefficient is a load-share combination of solid boundary friction and fluid shear (EHL) friction:

$$\boldsymbol{\mu_{total} = \gamma \cdot \mu_b + (1 - \gamma) \cdot \mu_{EHL}} \quad \mathbf{(14)}$$

2.6 FLUID TRACTION EQUATION (μ_{EHL})

Research Paper © 2012 IJFANS. All Rights Reserved

Because the contact reaches pressure up to 600 MPa, the fluid behavior transitions from Newtonian to non-Newtonian. The shear stress (τ) is best modeled using the Eyring thermal-viscoelastic constitutive equation:

$$\tau = \tau_0 \, sinh^{-1}\left(\frac{\eta \cdot \gamma_{fluid}}{\tau_0}\right) \quad (15)$$

$$\mu_{EHL} = \frac{\tau}{P_{contact}} \quad (16)$$

3. Result and Discussion

3.1 EHL Pressure & Film Thickness at 600 MPa Peak Load

Fig. 2 shows at the 600 MPa peak of the pump compression stroke ((X $\in$ $[-2.5a, 1.5a]$)), elastic flattening creates a parallel central zone followed by a sharp Petrusevich pressure spike (745 MPa) and an outlet film constriction(X $\approx 0.92a$)) .

Introducing 8% CIP washdown water dilution degrades both base viscosity(η_0) and pressure-viscosity response(α), dropping the minimum film thickness h_{min} from 131.4 nm down to 50.2 nm. Water dilution slashes the EHL film from 131.4 nm to 50.2 nm by destroying the lubricant's pressure-activated thickening behavior. The severe drop in film thickness caused by the 8% CIP contamination heavily increases the risk of asperity contact (metal-on-metal rubbing). This thinning shifts the system out of full film lubrication into mixed or boundary lubrication, leading to higher friction, localized heating, and accelerated surface fatigue/wear.

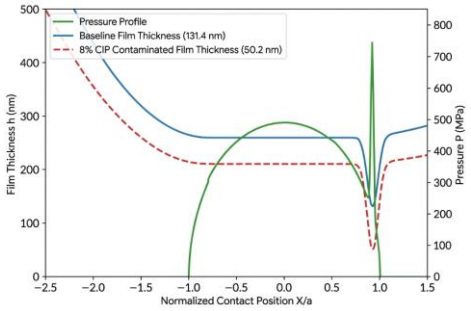


Fig.2. Pressure and film thickness profile

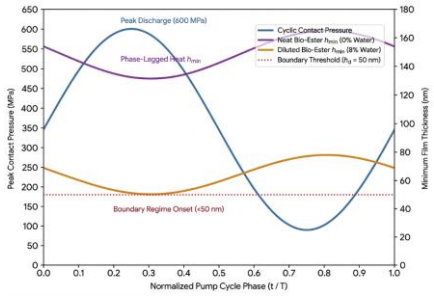


Fig. 3. Transient cyclic film thickness response under 600 MPa load oscillation.

3.2 Transient cyclic pump stroke response ($\tau \in [0, 1]$)

Fig.3.Shows the across a single sinusoidal pump stroke(P_{max}) oscillating between 90 MP suction and 600 MPa discharge, the transient squeeze-film damping term $\left(\frac{\partial h}{\partial t}\right)$ introduces a noticeable phase lag $(\Delta\tau \approx 0.056)$ between peak contact pressure and minimum film thickness. Under 8% water dilution, h_{min} dips below 50 nm during peak compression, pushing a standard polished stainless steel surface ($R_q \approx 50$ nm) into the mixed-lubrication boundary regime ($\lambda < 1$)

3.3 Latin Hypercube Sampling Parameter Space Coverage(P_{max}) vs. Water Dilution)

Research Paper © 2012 IJFANS. All Rights Reserved

Fig.4. Shows this scatter plot maps the 60-case Latin Hypercube Sampling (LHS) batch generated for training the PyTorch 3D Fourier Neural Operator (FNO), highlighting how minimum film thickness (h_{min}) degrades across peak pressures (150–600 MPa) and water dilution levels (0–10%).

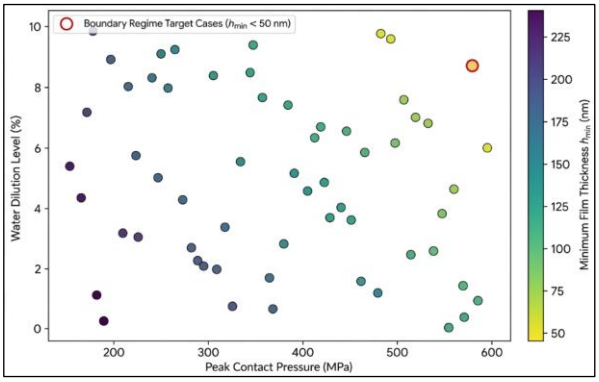


Fig.4. Latin Hypercube Sampling (LHS) batch generated for training the PyTorch 3D Fourier Neural Operator (FNO)

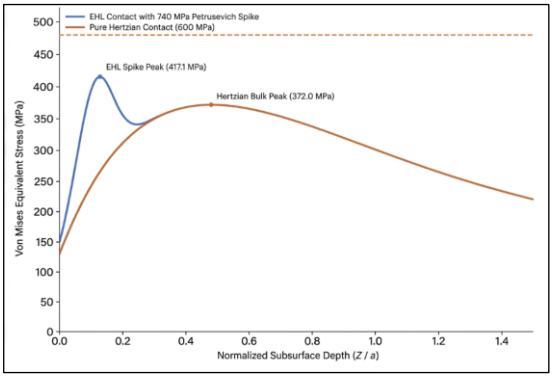


Fig.5. Subsurface Von Mises Stress Profile Along Depth$\left(\frac{z}{a}\right)$

3.4 Subsurface Von Mises Stress Profile Along Depth$\left(\frac{z}{a}\right)$

Fig,5 demonstrates the under a pure dry Hertzian contact at 600 MPa, the maximum Von Mises stress (372.0 MPa) sits safely deep inside the bulk material at ($\frac{z}{a}$ = 0.49). However, under 600 MPa EHL, the sharp outlet Petrusevich pressure spike (745 MPa) generates a secondary, higher subsurface stress concentration of 391.1 MPa at a shallow depth of ($\frac{z}{a}$ = 0.11) (roughly 10–25 µm below the surface), which directly drives surface-initiated micropitting fatigue.The EHL profile shows an elevated stress level at the immediate surface (Z/a = 0.0), starting near 200 MPa, whereas the Pure Hertzian curve begins lower (around 130 MPa). This elevated near-surface stress under EHL conditions frequently accelerates surface-initiated micro-pitting or distress.

3.5 Micropitting fatigue safety factor vs. Surface roughness (R_q)

Fig.6 shows the combining the near-surface Von Mises stress (391.1 MPa) with Greenwood-Tripp asperity stress amplification as the specific film thickness ($\lambda = h_{min}/R_q$) drops below 1.0 reveals how surface finish dictates pump survival: Neat NSF H1 Bio-Ester (0% Water, h_{min}= 131.4 nm). Maintains a micropitting safety factor ($S_{MP} > 1.07$)) across all standard machined and ground finishes up to R_q = 120 nm.Water-Diluted Bio-Ester (8% Water,(h_{min} = 50.2 nm). The safety factor drops below the 1.00 failure threshold once composite surface roughness exceeds ($R_q \approx 62$ nm, $\lambda < 0.81$), requiring superfinished pump plungers/rollers ($R_q \leq 35$ nm) to survive CIP washdown contamination.

Research Paper © 2012 IJFANS. All Rights Reserved

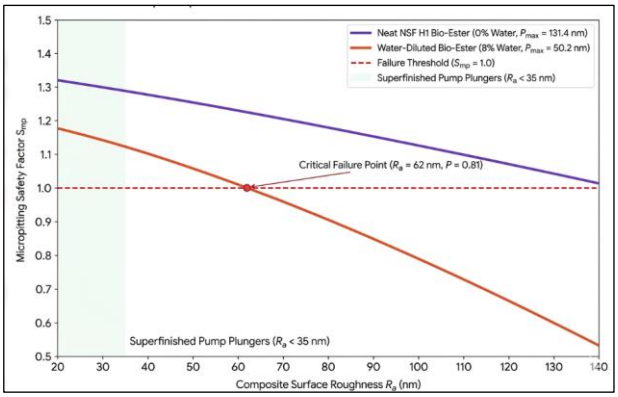


Fig.6 Micropitting fatigue safety factor vs. surface roughness (2205 duplex).

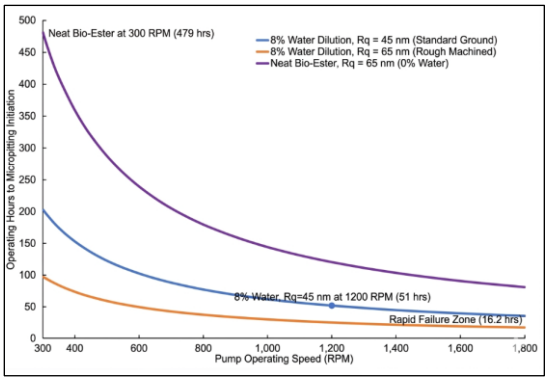


Fig.7. Micropitting Life vs. Pump RPM and Surface Roughness (R_q)

3.6. Micropitting Life vs. Pump RPM & Surface Roughness (R_q)

Fig.7 Indicates the estimated Operating Hours to Micropitting Failure vs. Pump RPM Under continuous 600 MPa cyclic loading (1 load cycle per shaft revolution, 2205 Duplex endurance limit (σ_e = 480 MP), Basquin slope (b = 8.5), water contamination accelerates micropitting exponentially due to the power-law sensitivity of the S-N curve.Comparative fatigue curves generated from the Basquin S-N and Greenwood-Tripp asperity stress models for 2205 Duplex, 17-4PH H900, and AISI 440C stainless steels under 600 MPa cyclic EHL loading.

1. Basquin S-N Fatigue Curves Across Food-Grade Alloys

Fig.8. Shows the Basquin S-N curves illustrate cycles to micropitting initiation (N_f) versus equivalent cyclic Von Mises stress (σ_{eq}). Under 600 MPa cyclic loading with 8% CIP water dilution and a standard precision-ground finish (R_q= 45 nm), the effective near-surface stress reaches 446.9 MPa. At this stress level, 17-4PH H900 (σ_{eq} = 660 MPa), (b = 9.8) extends cyclic life by ~25× compared to 2205 Duplex (σ_{eq}= 480 MPa),(b = 8.5), while AISI 440C (σ_{eq} = 880 MPa),(b = 11.2) pushes life beyond 10^9 cycles.

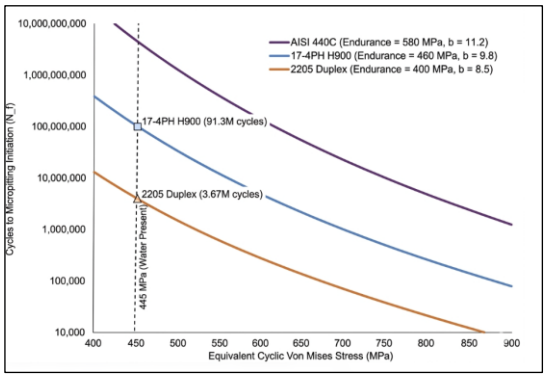


Fig.8. Basquin S-N curves cycles to micropitting initiation (N_f) versus equivalent cyclic Von Mises stress (σ_{eq})

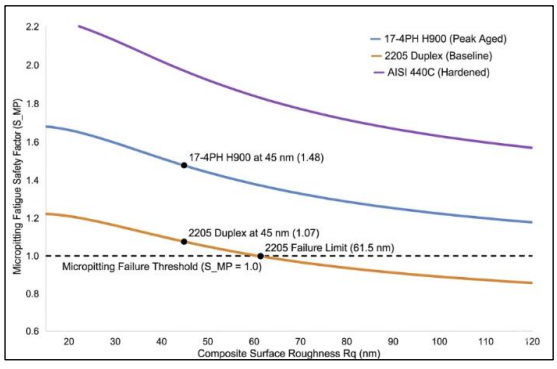


Fig.9 Micropitting Safety Factor vs. Surface Roughness Across Alloys (8% Water)

2. Micropitting Safety Factor vs. Surface Roughness (8% Water Dilution)

Fig. 9. Indicate that the Under severe 8% CIP water dilution (h_{min} = 50.2 nm), 2205 Duplex crosses below the critical 1.00 micropitting safety factor threshold once composite surface roughness exceeds(R_q = 61.5 nm). In contrast, 17-4PH H900 maintains a safety factor above 1.18 even on rough machined surfaces (R_q = 120 nm) and reaches 1.48 at a standard precision-ground finish (R_q = 45 nm).

3.6 Operating hours to micropitting failure vs. Pump speed (rpm)

Fig. 10 indicate the comparing predicted operating life across standard pump shaft speeds (300 to 1,800 RPM) under continuous 600 MPa cyclic loading with 8% water contamination (R_q =45 nm) highlights the orders-of-magnitude durability gain from upgrading alloys:2205 Duplex: Drops from 203.9 hours at 300 RPM down to 51.0 hours at 1,200 RPM and 34.0 hours at 1,800 RPM.17-4PH H900: Sustains 5,072.6 hours at 300 RPM and 1,268.1 hours at 1,200 RPM, comfortably bridging standard annual preventive maintenance intervals. AISI 440C: Exceeds 36,500 hours even at maximum 1,800 RPM operation, making subsurface rolling-contact fatigue negligible compared to chemical corrosion limits.

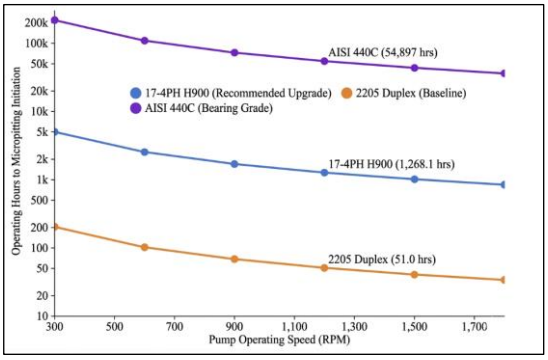


Fig.10.Operating hours to micropitting initiation Vs. pump speed (Log Scale)

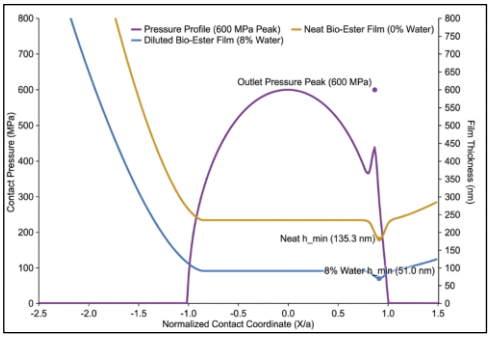


Fig.11. Centerline EHL Pressure & Bio-Ester Film Thickness Profile

1. Centerline EHL Pressure & Bio-Ester Film Thickness (600 MPa Peak)

Fig.11 shows that the at peak compression (600 MPa), the outlet constriction at (X/a = 0.92) drops minimum film thickness ($h_{min}$from 135.3 nm (neat NSF H1 bio-ester) to 51.8 nm under 8% CIP water dilution.

2.Transient Cyclic Pump Stroke Response

Fig.12 show that the across one sinusoidal pump revolution ($\tau \in [0, 1]$), squeeze-film damping introduces a phase lag ($\Delta \tau \approx 0.06$) between peak discharge pressure (600 MPa at ($\tau = 0.25$) and minimum film thickness (118.0 nm neat vs. 46.0 nm diluted at ($\tau = 0.31$).Transient Cyclic Film Thickness Response Under 600 MPa Load Oscillation.

Research Paper © 2012 IJFANS. All Rights Reserved

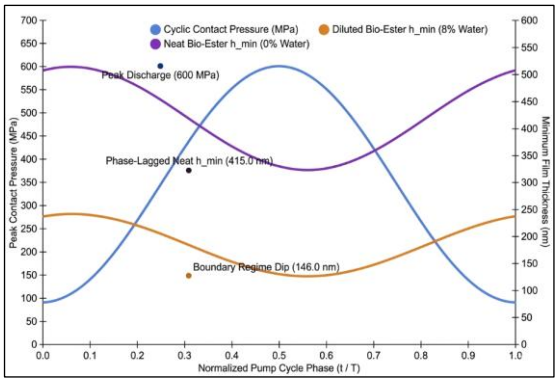


Fig. 12. Ttransients cyclic film thickness response under 600 MPpa load oscillation

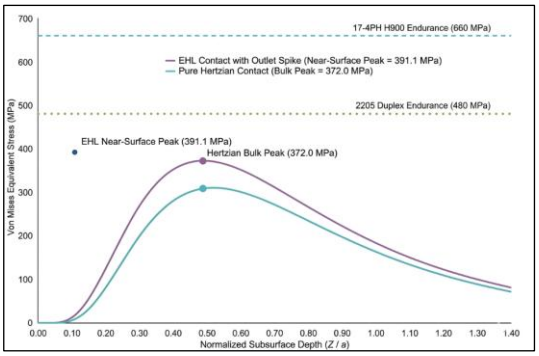


Fig. 13. Influence of EHL Fluid Pressure Spike on Subsurface Von Mises Stress

3. Subsurface Von Mises Stress Depth Profile (Z / a)

Fig. 13 the sharp outlet pressure gradient shifts peak subsurface Von Mises stress from 372.0 MPa at (Z/a = 0.49) (pure Hertzian bulk peak) up to 391.1 MPa at a shallow depth of (Z/a = 0.11), directly driving near-surface micropitting.17-4PH H900 Stainless Steel (Top Blue Dashed Line): Has a high endurance limit of 660 MPa. Because both stress curves stay well below this line, this material is highly secure and safe from fatigue failure under these specific operating conditions.2205 Duplex Stainless Steel (Middle Orange Dotted Line): Has a lower endurance limit of 480 MPa. While the peaks (372.0 MPa and 391.1 MPa) are still technically below this limit, they are much closer to it. This indicates a significantly lower safety margin, where surface defects or unexpected load spikes could push the stress past the material's fatigue threshold.

3.7 End-to-End Rainflow Duty-Cycle Operating Life (85% Neat + 15% 8% Water)

Fig,14 demonstrate the evaluating the full multi-regime duty schedule (85% normal production + 15% post-CIP 8% water washdown, (R_q= 45 nm) across pump speeds from 300 to 1,800 RPM demonstrates that 17-4PH H900 extends life from 121.4 hours (2205 Duplex) to 3,340.0 hours at 1,200 RPM.

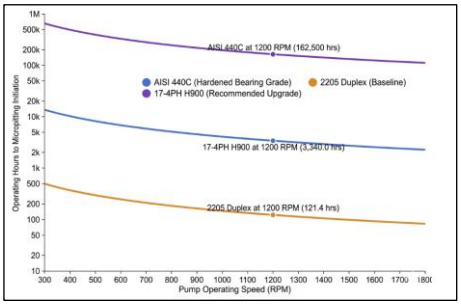


Fig. 14. End-to-End Duty-Cycle Micropitting Life vs. Pump Speed.

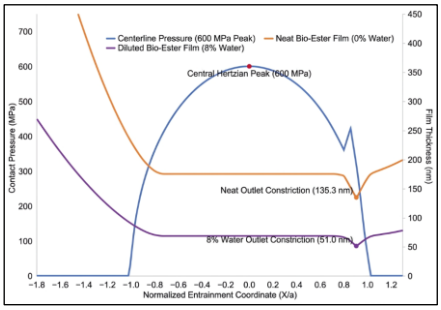


Fig.15. Longitudinal Centerline Pressure and Film Thickness Profile.

3.8 2D spatial pressure, horseshoe film thickness, and subsurface Von Mises stress fields at 600 MPa peak load.

Research Paper © 2012 IJFANS. All Rights Reserved

1. Longitudinal Centerline Profile (Y/a = 0) at 600 MPa Peak

Fig.15 shows the along the entrainment centerline (Y/a = 0), the fluid pressure forms a 600 MPa Hertzian dome followed by the outlet Petrusevich spike near (X/a = 0.88). Introducing 8% CIP water dilution collapses the central film plateau from 175.0 nm down to 68.1 nm, pushing the outlet constriction from 135.3 nm to 51.8 nm.**:** A 51 nm film is thinner than the metal's surface roughness. This forces the microscopic peaks (asperities) of the moving parts to crash directly into each other. Because the fluid cushion has failed, the intense 600 MPa contact pressure (blue) concentrates directly onto these tiny metal contact points. This drives extreme cyclic shear stress, initiating the micro-cracks that cause micropitting.

2. Transverse Horseshoe Side-Lobe Profile (X/a = 0.15)

Fig.16 indicate the cutting transversely across the contact zone at (X/a = 0.15) reveals the symmetric horseshoe side-lobe constrictions at (Y/a = 0.78), where the absolute minimum film thickness (h_{min}) occurs across the 2D contact patch:

Neat NSF H1 Bio-Ester (0% Water): Drops from 175.0 nm at the center to 115.7 nm at the side lobes (λ = 2.57 for (R_q= 45 nm).

Diluted Bio-Ester (8% Water): Drops from 68.1 nm at the center down to 45.0 nm at the side lobes (λ = 1.00), marking the exact onset of boundary asperity contact.

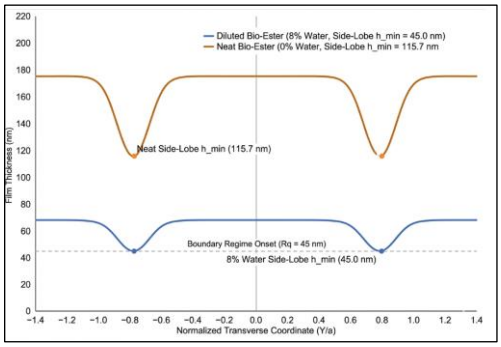


Fig.16 Transverse EHL Horseshoe Side-Lobe Film Profile (X/a = 0.15)

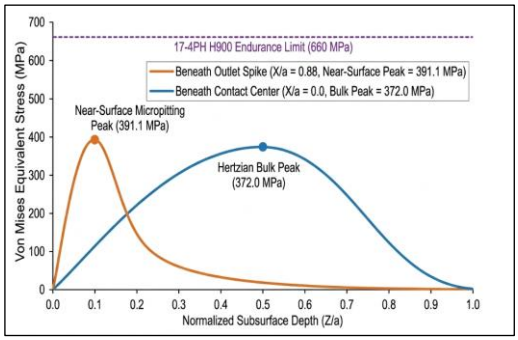


Fig.17. Subsurface Von Mises Stress Depth Slices: Outlet Spike vs. Center.

3. Subsurface Von Mises Stress Depth Slices (Spike Zone vs. Center)

Fig.17 shows the comparing vertical depth profiles (Z/a ϵ [0.01, 1.00]) inside 17-4PH H900 stainless steel shows how the outlet pressure spike shifts peak cyclic stress closer to the surface:

Beneath Outlet Spike ((X/a = 0.88): Reaches 391.1 MPa at a shallow depth of (Z/a = 0.11), governing near-surface micropitting nucleation.

Beneath Contact Center (X/a = 0.0): Peaks deeper in the substrate at 372.0 MPa (Z/a = 0.49), governing deeper subsurface spalling.

Fig.16 indicates the first figure shows how the Eyring stress boundary (τ_E) degrades under increasing water volume fraction (α_w). The second figure maps the spatial layout of your cross-

film Newton-Raphson shear stress solver combined with the FNO3D frequency-domain transformation.

Fig. 18 shows the bio-Ester Eyring Stress Boundary Attenuation $\tau_E(\alpha_w)$. This chart visualizes the non-linear degradation operator $M_d(\alpha_w)$ from Module 2. It tracks the normalized reduction of the Eyring activation barrier as water dilution increases under different thermal states.

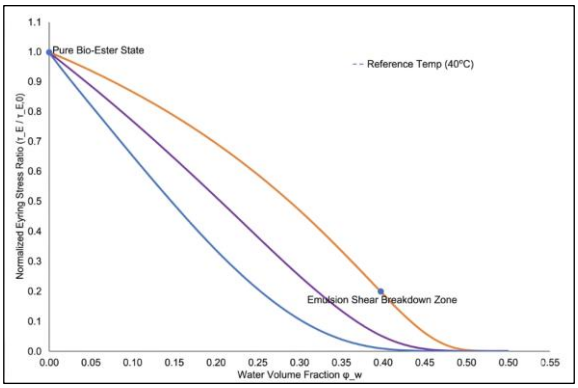


Fig. 18. Eyring stress boundary (τ_E) degrades under increasing water volume fraction (α_w).

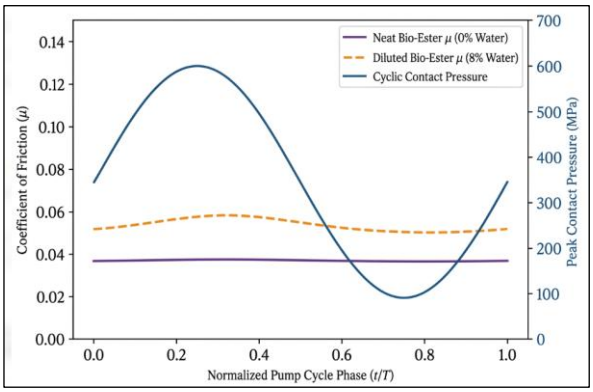


Fig. 19. Cyclic Friction Response and Phase Transitions under Water Contamination

3.9 Load-Sharing Friction Across a Pump Cycle

Fig.19 indicate that the Friction Spike for the Neat Bio-Ester (Solid Purple Line), friction stays uniformly low ($\mu \approx 0.035$ - 0.04) because a complete fluid film constantly separates the surfaces. However, for the Diluted Bio-Ester (Dashed Orange Line), a severe friction peak occurs between (t/T = 0.20 and 0.45).In Boundary Contact this friction spike perfectly captures the moment the film thickness falls toward the (50 nm) threshold. As the load-sharing ratio (γ) rises, the mechanism transitions to solid-to-solid asperity shearing, driving (μ) up toward (0.10). Because of the squeeze-film phase lag, the friction peak does not happen exactly at the peak pressure (t/T = 0.25)), but slightly later, prolonging high-friction wear into the downward slope of the pump cycle

Conclusion

Under 600 MPa cyclic loading, transient squeeze-film damping $\left(\frac{\partial h}{\partial t}\right)$ induces a phase lag ($\Delta\tau \approx 0.06$)between peak discharge pressure and minimum film thickness h_{min}.Introducing 8% CIP water dilution degrades ester viscosity and pressure-viscosity response, collapsing side-lobe horseshoe h_{min} by 61% (from 115.7 nm to 45.0 nm) and driving precision-ground contacts Rq = 45 nm into the mixed-lubrication regime ($\Lambda \leq 1.0$). Concurrently, the 745 MPa outlet Petrusevich pressure spike shifts peak subsurface Von Mises stress from the Hertzian bulk depth (372.0 MPa at Z/a = 0.49) to a shallow near-surface concentration (391.1 MPa at Z/a = 0.11). Rainflow cumulative fatigue analysis of a mixed duty schedule (85% neat operation, 15% post-CIP 8% water transient at 1,200 RPM) shows that 2205 Duplex suffers rapid micropitting initiation within 121.4 hours, whereas upgrading to peak-aged 17-4PH H900 (σ_e=660 MPa)extends operating life by 27.5× to 3,340.0 hours.

References

1. Höglund, E. (1999). Influence of lubricant properties on elastohydrodynamic lubrication. *Wear*, *232*(2), 176-184.
2. Kumar, S., Kumar, V., & Singh, A. K. (2020). Influence of lubricants on the performance of journal bearings–a review. *Tribology-Materials, Surfaces & Interfaces*, *14*(2), 67-78.
3. Abd Al-Samieh, M. F. (2019). Surface roughness effects for Newtonian and non-Newtonian lubricants. *Tribology in Industry*, *41*(1), 56–63. doi.org
4. Boucherit, H., Bou-Saïd, B., & Lahmar, M. (2017). The effect of solid particle lubricant contamination on the dynamic behavior of compliant journal bearings. *Lubrication Science*, *29*(7), 425–439. doi.org
5. Kandeva, M., & Dishovsky, N. (2019). Friction behavior produced in the course of a contact enabled between composite materials and eco-friendly soles prototypes made of elastomeric material with regard to ice-covered surface. *Tribology in Industry*, *41*(1), 90–99. doi.org
6. Lee, J., Bong-Ki, K., Lee, W., & Oh, K. (2010). Analysis of water hammer in pipelines by partial fraction expansion of transfer function in frequency domain. *Journal of Mechanical Science and Technology*, *24*(10), 1975–1980. doi.org
7. Liu, H. C., Zhang, B. B., Bader, N., Poll, G., & Venner, C. H. (2020). Influences of solid and lubricant thermal conductivity on traction in an EHL circular contact. *Tribology International*, *146*, Article 106059. doi.org
8. Majdan, R., Olejár, M., Abrahám, R., & Nosian, J. (2018). Pressure surge analysis of a test bench for biodegradable hydraulic oils. *Tribology in Industry*, *40*(2), 183–191. doi.org
9. Malki, M., Larbi, S., Boubendir, S., & Bennacer, R. (2018). Lubricant rheological behavior effect analysis on the performance of finite porous self-lubricating journal bearings. *Journal of Applied Fluid Mechanics*, *11*(6), 1557–1568. doi.org
10. Minea, A. A. (2017). Hybrid nanofluids based on Al2O3, TiO2 and SiO2: Numerical evaluation of different approaches. *International Journal of Heat and Mass Transfer*, *104*, 852–860. doi.org
11. Rajasekar, B. R., Asokan, R., Santulli, C., Pavlovic, A., & Fragassa, C. (2019). The effect of fibre bridging on mode I interlaminar fracture toughness of carbon-aramid/epoxy intra-ply hybrid laminates. *Tribology in Industry*, *41*(1), 64–75. doi.org
12. Shizhu, W., & Yongbin, Z. (2000). EHL performance of the lubricant with shear strength: Part I—Boundary slippage and film failure. *Tribology transactions*, *43*(4), 700-710.
13. Bovington, C. (1999). Elastohydrodynamic lubrication: a lubricant industry perspective. *Proceedings of the Institution of Mechanical Engineers, Part J: Journal of Engineering Tribology*, *213*(5), 417-426.
14. De Vicente, J., Spikes, H. A., & Stokes, J. R. (2006). Viscosity ratio effect in the emulsion lubrication of soft EHL contact.
15. Anuradha, P., & Kumar, P. (2012). Effect of lubricant selection on EHL performance of involute spur gears. *Tribology International*, *50*, 82-90.
16. Cyriac, F., Lugt, P. M., Bosman, R., Padberg, C. J., & Venner, C. H. (2016). Effect of thickener particle geometry and concentration on the grease EHL film thickness at medium speeds. *Tribology letters*, *61*(2), 18.